

Fermi surface investigation of the semimetal TaAs₂

Butcher, T.; Hornung, J.; Förster, T.; Uhlarz, M.; Klotz, J.; Sheikin, I.; Wosnitza, J.;
Kaczorowski, D.;

Originally published:

June 2019

Physical Review B 99(2019), 245112

DOI: <https://doi.org/10.1103/PhysRevB.99.245112>

Perma-Link to Publication Repository of HZDR:

<https://www.hzdr.de/publications/Publ-29393>

Release of the secondary publication
on the basis of the German Copyright Law § 38 Section 4.

Fermi-surface investigation of the XMR semimetal TaAs₂

T. A. Butcher,^{1,2,*} J. Hornung,^{1,2} T. Förster,¹ M. Uhlarz,¹ J. Klotz,¹ I. Sheikin,³ J. Wosnitza,^{1,2} and D. Kaczorowski⁴

¹*Hochfeld-Magnetlabor Dresden (HLD-EMFL), Helmholtz-Zentrum Dresden-Rossendorf, 01328 Dresden, Germany*

²*Institut für Festkörper- und Materialphysik, Technische Universität Dresden, 01062 Dresden, Germany*

³*Laboratoire National des Champs Magnétiques Intenses (LNCMI-EMFL), CNRS, UGA, 38042 Grenoble, France*

⁴*Institute of Low Temperature and Structure Research,
Polish Academy of Sciences, 50-950 Wrocław, Poland*

(Dated: April 12, 2019)

The transversal magnetoresistance associated with the semimetal TaAs₂ shows a parabolic field dependence that rises unrestrictedly to 2800 at 14 T and 1.8 K. Here, we report on a comprehensive quantum-oscillation study. We obtained angular-dependent de Haas-van Alphen (dHvA) data with the method of cantilever-torque magnetometry and compared them with the results of density functional theory calculations. These were carried out with the full-potential nonorthogonal localized-orbital band-structure scheme and predict a Fermi surface with two kinds of electron pockets as well as two types of hole pockets. Only the electron pockets could be experimentally verified, whereas no evidence for the hole pockets is present in the measured dHvA frequencies.

I. INTRODUCTION

The present flurry of research activity in the field of topological semimetals has ignited the study of the magnetoresistive properties of a large number of alloys. Recently, a multitude of such investigations for the class of transition-metal dipnictide semimetals have appeared^{1–7}. One member of this family is TaAs₂ which has a monoclinic structure and is diamagnetic^{8,9}. Several authors report the existence of an extremely large magnetoresistance (XMR) with a parabolic field dependence that does not saturate for TaAs₂^{3–6}. This behavior can be ascribed to the phenomenon of electron-hole compensation in semimetals^{10,11}. The occupation of the electron and hole band is directly linked to the presence of the corresponding Fermi-surface pockets. Consequently, the importance of the exact determination of the Fermi surface and verification of calculated band structures is self-evident. Furthermore, claims of magnetic field induced Weyl points in TaAs₂¹² and the hosting of Dirac nodal-lines in the sister compound NbAs₂¹³ have been made. These merit further experimental investigation of the electronic structure. The magnetoresistance publications contain calculated band structures and predicted Fermi surfaces, but no experimental evidence^{3–6}. Hitherto, only the Fermi surface of NbAs₂ has been experimentally analyzed¹ while experimental data for TaAs₂ is lacking. Here, we present a detailed Fermi-surface investigation of TaAs₂, combining both measurements of the de Haas-van Alphen (dHvA) effect and density-functional theory (DFT) calculations using the FPLO code.

II. EXPERIMENTAL DETAILS

Single crystals of TaAs₂ were grown by the chemical vapor transport method using iodine as a transport agent, following the recipe described in Ref. [6]. The obtained platelet-like crystals of typical sizes of

$3 \times 1 \times 0.2$ mm³ had metallic luster and appeared stable against air and moisture. TaAs₂ occurs with a centrosymmetric base-centered monoclinic crystal structure and space group $C2/m$ (#12), which possesses a two-fold symmetry around the $[010]$ axis. All crystals were plate-like, with the $[010]$ axis parallel to the long edge of the sample and the $[\bar{2}01]$ pointing out of the flat plane of the plate, similar to those reported in Ref. [14]. Resistivity measurements were performed with a standard four-probe technique in a commercial Quantum Design physical properties measurement system, with current flowing parallel to the b axis. All four contacts were placed parallel, as described in Ref. [6], in order to avoid side effects resulting from current jetting^{15–18}. Angle-dependent quantum-oscillation measurements were performed using capacitive torque magnetometry, employing 50 μ m thick CuBe cantilevers. These experiments were conducted in superconducting magnet systems equipped with a dilution refrigerator and a ³He system, reaching 18 T/30 mK and 13 T/350 mK, respectively.

III. RESISTIVITY MEASUREMENTS

Figure 1(a) shows the temperature dependence of resistivity, ρ , at temperatures down to 1.8 K, for zero and applied magnetic field. In zero field, the resistivity follows a metallic behavior, decreasing monotonically with decreasing temperatures until 15 K, where it reaches its impurity-scattering-induced low-temperature limit. A double-logarithmic plot of $\rho(T)$, as shown in the inset of Fig. 1(a), reveals a dependence $\rho(T) = \rho(0) + aT^n$ below 100 K. From a fit to the data, we obtain a residual resistivity of $\rho(0) \approx 8 \cdot 10^{-7}$ Ω cm and an exponent $n \approx 2.4$, larger than the value expected for a Fermi-liquid behavior ($n = 2$), but smaller than reported by Yuan et al. ($n = 2.7 \dots 3.0$)⁶. Towards higher temperature, the exponent decreases and the resistivity approaches a $\rho \propto T$ dependence near room temperature. In contrast to this metallic behavior at zero field, at 14 T there is only a 10%

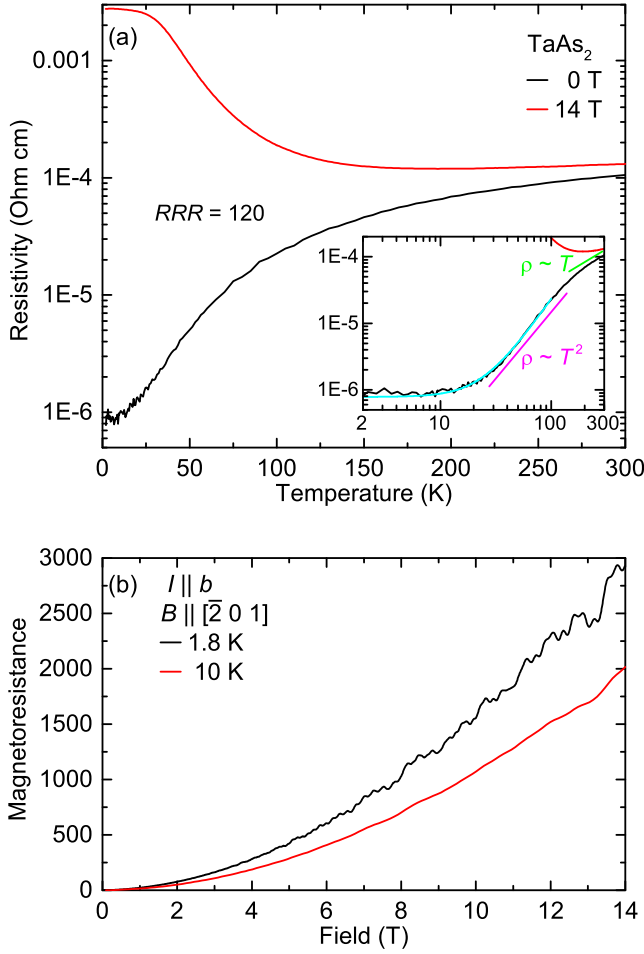


FIG. 1. (a) Temperature dependence of the resistivity, at zero field and an applied field of 14 T. Inset: log-log plot highlighting different $\rho(T)$ regimes. The green and magenta lines are guides for the eyes indicating slopes of a linear and a quadratic behavior, respectively. The cyan line is a power-law fit $\rho(T) = \rho(0) + aT^n$ to the zero-field data below 100 K. (b) Magnetoresistance of TaAs₂, expressed as $\Delta\rho/\rho(B=0)$. SdH oscillations appear at fields larger than 4 T.

decrease of resistivity when cooling from room temperature down to 200 K. Upon further cooling, the resistivity increases to about $20 \times \rho(300 \text{ K})$ at 20 K and remains constant at lower temperatures. A similar behavior was also observed in previous studies of TaAs₂ and other semimetals (see Refs. [4–6] and references therein). From the zero-field data, we deduce a residual resistivity ratio $RRR = \rho(300 \text{ K})/\rho(1.8 \text{ K}) \approx 120$, indicating an excellent sample quality. Other samples from the batch exhibited values up to $RRR = 130$, further substantiating the high quality of our samples.

For our magnetoresistance measurements, we applied the current I along the crystallographic b axis, while the magnetic field was aligned parallel to the $[\bar{2}01]$ axis, hence $B \perp I$. The resulting magnetoresistance, $MR(B) = [\rho(B) - \rho(0)]/\rho(0)$, is depicted in Fig. 1(b). For the entire field range investigated, we observe a roughly

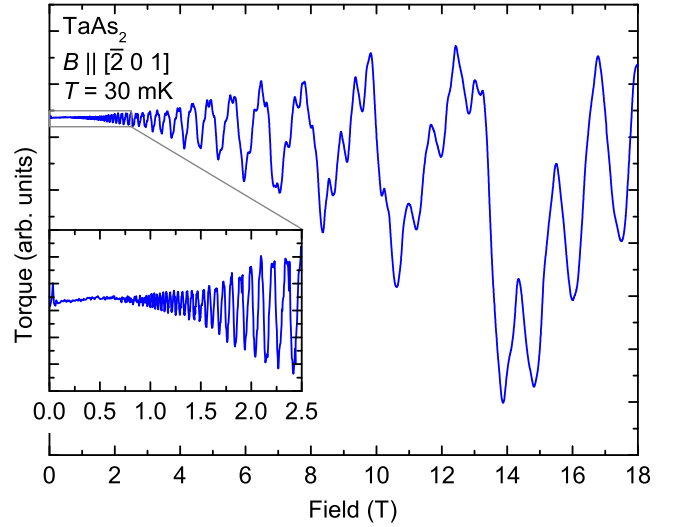


FIG. 2. Field-dependent torque magnetization measured close to $B \parallel [\bar{2}01]$. The inset is the enlarged low-field region in which quantum oscillations appear at approximately 0.7 T.

parabolic, non-saturating $MR(B)$ behavior. At 14 T and 1.8 K, we find a value of $MR \approx 2800 = 2.8 \cdot 10^5\%$. This value is of the same order of magnitude as the best samples reported by Yuan et al.⁶ and Wang et al.⁵, but about two orders of magnitudes less than reported by Wu et al.⁴. Additionally, Shubnikov-de Haas (SdH) oscillations were observed above 4 T. The corresponding SdH frequencies will be discussed in the next section. The sample characterization through field- and temperature-dependent resistivity measurements assure a high sample quality. Thus, deviations of the sample's properties due to impurities or vacancies are expected to be negligible. Especially, a sizeable shift of the Fermi energy, E_F , because of vacancy-induced doping seems unlikely.

IV. DE HAAS-VAN ALPHEN EFFECT

Figure 2 shows a typical as-measured torque signal, taken at 30 mK and $B \parallel [\bar{2}01]$. Quantum oscillations are clearly visible and the non-oscillatory background is comparatively small. We were able to resolve oscillations at fields as low as 0.7 T, as can be seen in the inset of Fig. 2. A polynomial background subtraction and Fourier transformation yields the frequency spectrum displayed in Fig. 3. Besides the dominant low-frequency peak of F_1 , we observed two additional high-amplitude frequencies, labeled F_2 and F_3 , and several higher harmonics. When zooming in on the high-frequency part of the spectrum, a higher dHvA frequency (F_5) and more harmonics become discernible. The abundance of harmonics in the frequency spectra complicates the data analysis, necessitating a thorough and diligent approach.

A comparison between the SdH frequencies obtained from the MR and the dHvA measurements can be made.

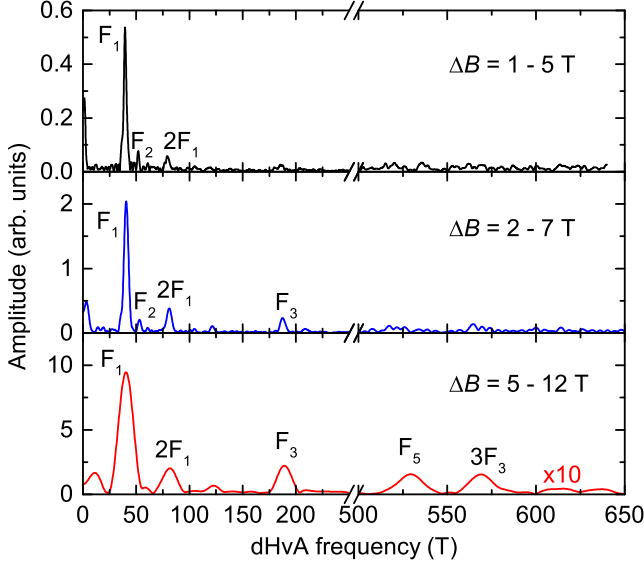


FIG. 3. Frequency spectrum corresponding to the data of Fig. 2, obtained after polynomial background subtraction and subsequent Fourier transformation. At higher fields, up to four different frequencies are resolved.

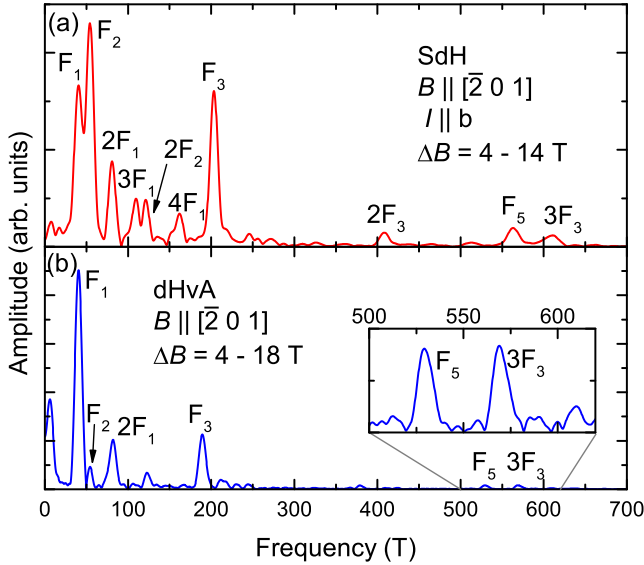


FIG. 4. Frequency spectra measured by (a) SdH at 1.8 K and (b) dHvA at 30 mK with $B \parallel [\bar{2}01]$.

This is presented in Fig. 4 for $B \parallel [\bar{2}01]$. Both SdH and dHvA measurements concur in the number of observed frequencies. The agreement between the two low frequencies (F_1 and F_2) is excellent, whereas slight relative differences between F_3 and F_5 are present ($\approx 8\%$ for F_3 and $\approx 6\%$ for F_5). These discrepancies can be explained by subtle differences in the field orientation. There are also different relative oscillation amplitudes, which are expected for different techniques and temperatures. Additionally, we measured dHvA oscillations in a

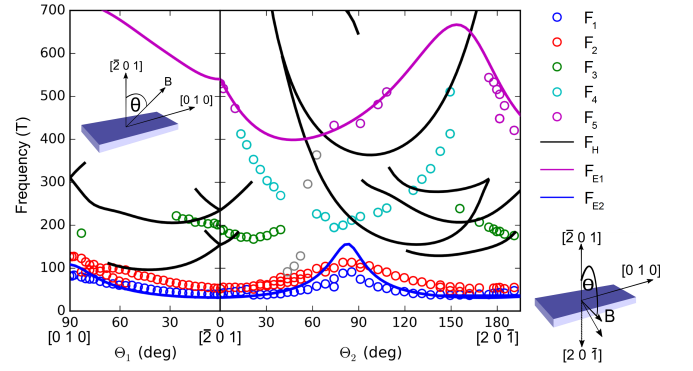


FIG. 5. Angular dependence of the measured (circles) and theoretical (lines) dHvA frequencies of TaAs₂. The left part shows the 90° rotation from the b to the $[\bar{2}01]$ axis and the right the 180° rotation in the ac -plane (see sketches illustrating the sample geometry). The grey circles indicate dHvA frequencies that could not be designated to a specific branch. Colors of the calculated frequencies correspond to the Fermi surface colors in Fig. 7.

second sample from the same batch for the main orientations, $B \parallel [\bar{2}01]$ and $B \parallel [010]$. All dHvA frequencies of both samples agree within error bars (not shown). Consequently, a significant sample dependence of our results is unlikely.

The full angular dependence of the dHvA frequencies is shown in Fig. 5. This was recorded from $B \parallel [\bar{2}01]$ to $B \parallel [010]$ and from $B \parallel [\bar{2}01]$ to $B \parallel [20\bar{1}]$ which is illustrated with the sketches in Fig. 5. Both F_1 and F_2 frequency branches are present at all angles, while F_3 frequencies are encountered around 200 T close to the orientation of the magnetic field in $[\bar{2}01]$ direction. Comparatively higher frequencies (200 to 570 T) emerge for the rotation around the b axis and are assigned to a fourth and fifth frequency branch F_4 and F_5 . The two low-frequency branches have a common maximum 82° from the $[\bar{2}01]$ direction in the ac -plane and are otherwise almost completely parallel with little angular variation. None of the observed frequencies exceed 570 T, which can be seen as a manifestation of small electron or hole pockets, as expected for semimetallic compounds.

Due to the small effective masses and the limited range in which the dilution refrigerator temperatures could be stabilized, we measured the temperature dependence of the dHvA frequency amplitudes in a ^3He cryostat, combined with a magnet with a maximum field of 15 T. Temperature dependences were obtained for orientation of the magnetic field in b and $[\bar{2}01]$ direction. Only the two dominant low frequencies F_1 and F_2 were detectable. The corresponding effective masses m_1^* and m_2^* were found by fitting the temperature damping factor R_T of the Lifshitz-Kosevich formula¹⁹ to the oscillation amplitudes with respect to temperature. The damping factor can be expressed as $R_T = x / \sinh(x)$, with $x = \alpha m^* T / B$, $\alpha = 2\pi^2 k_B m_e / (e\hbar) \approx 14.69 \text{ T/K}$, and m^* the effective mass in units of the free electron mass, m_e . Here, k_B re-

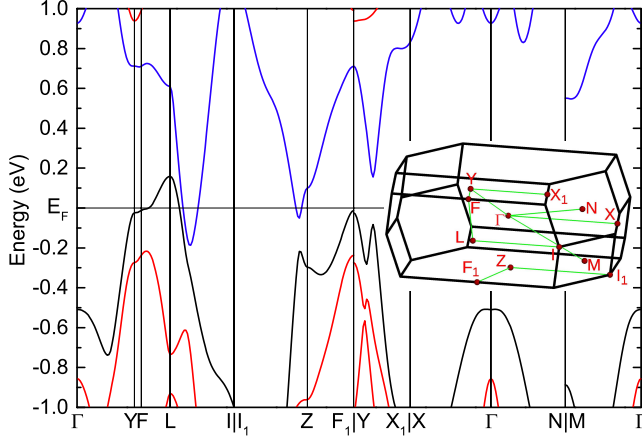


FIG. 6. Calculated band structure of TaAs₂. The inset shows the first Brillouin zone with high-symmetry points. One hole band (black) and one electron band (blue) cross Fermi energy (E_F).

presents the Boltzmann constant, e the electron charge, and \hbar the reduced Planck constant. The resulting effective masses are summarized and compared with the values resulting from first-principles calculation in Tab. I (next section).

V. FERMI-SURFACE CALCULATIONS

A rigorous analysis of the Fermi surface relies on the results of DFT calculations which were performed with the FPLO code (version 15.02-50)²⁰. The generalized gradient approximation (GGA) by Perdew, Burke and Ernzerhof²¹ was used for the exchange-correlation functional and the structural parameters reported by Ling et al.²² were deemed to be the literature experimental values. Numerical optimization barely changes the relative internal atomic positions. Subsequently, all calculations were performed with meshes of $16 \times 16 \times 16$ k points using the experimental lattice constants as input.

The band structure was calculated with a fully relativistic setting taking spin-orbit coupling (SOC) into account (see Fig. 6). One electron- and one hole band cross the Fermi level which is a prerequisite for charge compensation. Band crossings do not materialize in the band-structure calculation upon inclusion of SOC. Thus, the possibility of TaAs₂ being a Dirac semimetal can be ruled out.

The resulting Fermi surface (see Fig. 7) agrees well with previous publications^{23,24}. Three different pocket shapes are present: (I) One hole pocket H centered at the L point which resembles an elliptical shape with two “antlers” attached to it [Figs. 7(a) and 7(b)], (II) two elliptical electron pockets E_1 to each side of the H pocket and the L point [Fig. 7(c)], and (III) two small elliptical electron pockets E_2 around the Z point [Fig. 7(d)].

Theoretical dHvA frequencies were extracted from the

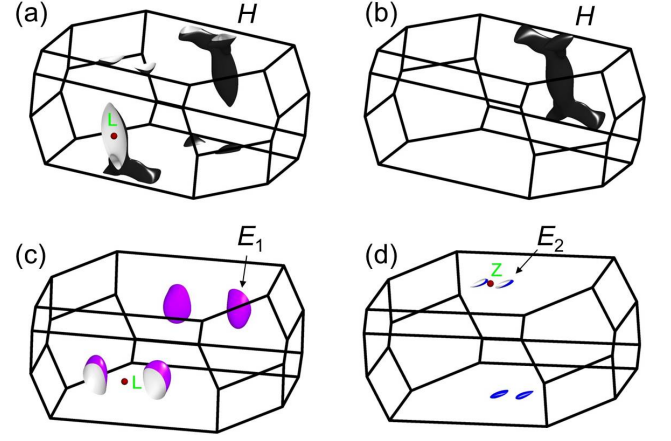


FIG. 7. Calculated Fermi-surface sheets of (a) hole pocket H , (c) electron pocket E_1 , and (d) electron pocket E_2 . (b) shows the same pocket as (a), but not restricted to the first Brillouin zone.

extremal Fermi-surfaces cross sections and are shown together with the experimental data in Fig. 5. The behaviors of F_1 , F_2 , and F_5 are reflected by the DFT calculations. Although only one low-frequency branch is predicted by the theory, its angular dependence matches that of F_1 and F_2 with a maximum at 82° from $[\bar{2}01]$. This is ascribed to the small E_2 electron pockets close to the Z point of the Brillouin zone [see Fig. 7(d)]. In principle, the Fermi-surface pocket associated with F_2 must be a slightly larger version of E_2 . The frequencies due to the E_1 electron pockets follow the F_5 branch. Glaring discrepancies exist between the rest of the theoretical dHvA frequencies and the experimental results. The calculations miss the flat F_3 branch close to $B \parallel [\bar{2}01]$ entirely and feature a high number of unobserved frequency branches ascribed to the hole pocket H . Notably, the high frequencies pertaining to H are unaccounted for by the experiment. Consequently, it is highly likely that the shape of the hole band is incorrectly described by the DFT calculations. One possible reason for discrepancies between experiment and theory might be slight deviations from perfect stoichiometry, which would cause small changes in Fermi energy. Our calculations with shifted Fermi energies were accompanied by enlargement or shrinkage of the respective Fermi surface pockets. However, this did nothing to alleviate the discrepancy between theory and experiment.

When comparing our results on TaAs₂ to the isoelectronic NbAs₂¹, some similarities become obvious. Both compounds feature one electron and one hole band at the Fermi energy^{1,25,26}. While NbAs₂ possesses electron pockets similar to the TaAs₂ electron pockets E_1 and E_2 , the hole pocket H of TaAs₂ is separated into smaller hole pockets in NbAs₂. Furthermore, there is also a discrepancy between quantum-oscillation data and calculated frequencies, which in NbAs₂ could be partially resolved by globally rescaling the calculated frequencies

TABLE I. Experimental dHvA frequencies (F_1 and F_2) and effective masses (m_1^* and m_2^*), in comparison to theoretical frequencies (F_{DFT}) and band masses (m_b), for two orientations of the magnetic field.

orientation	Frequency (T)			Mass (m_e)		
	F_{DFT}	F_1	F_2	m_b	m_1^*	m_2^*
$B \parallel [010]$	108	85	130	0.27	0.45	0.44
$B \parallel [\bar{2}01]$	32	41	54	0.09	0.20	0.35

by a constant factor.

Band masses m_b were extracted from the DFT calculation and are listed next to the experimental values in Tab. I. For F_1 and F_2 , the effective masses $m_1^* = 0.45 m_e$ and $m_2^* = 0.44 m_e$ are nearly identical for $B \parallel [010]$. These low effective masses are expected for semimetals with small Fermi surface pockets. For $B \parallel [\bar{2}01]$, the effective masses $m_1^* = 0.2 m_e$ and $m_2^* = 0.35 m_e$ are diminished. This is also expected, since in first approximation, the effective masses of different extremal orbits of the same pocket are proportional to the area of the orbits, which are in turn proportional to the dHvA frequencies. For F_1 , both frequency and mass differ by a factor of two between the two directions investigated. As previously discussed, only one of the low frequencies is predicted by the calculations and the pertaining band mass m_b also differs by a factor of two between the two directions, in agreement with experiment. The absolute values, however, differ by a factor of two. This can be explained by many-body effects, which are omitted in calculations and

which enhance effective masses.

VI. SUMMARY

Measurement of the dHvA effect in TaAs₂ revealed five distinct dHvA frequency branches. The band structure was calculated with the FPLO method of DFT and showed one electron and one hole band crossing the Fermi level. The dHvA measurements and DFT calculations were able to consistently identify two Fermi-surface pockets ascribed to the electron band. However, serious discrepancies prevailed between the majority of the experimental and theoretical data. The transverse MR exhibited a parabolic field dependence up to nearly $3 \times 10^5\%$ and undergoes no saturation at 14 T. This suggests electron-hole compensation as the prevalent mechanism for the MR, as has been previously inferred from measurements of the Hall effect^{4,5}. However, the insufficient agreement between experimental data and DFT calculations cannot provide further evidence for electron-hole compensation. Consequently, more sophisticated theoretical methods are required to fully understand the electronic structure of TaAs₂.

VII. ACKNOWLEDGMENTS

We acknowledge support by HLD at HZDR, member of the European Magnetic Field Laboratory (EMFL), from the ANR-DFG grant “Fermi-NES_t”, and from the DFG through the Würzburg-Dresden Cluster of Excellence on Complexity and Topology in Quantum Matter – *ct.qmat* (EXC 2147, project-id 39085490). We thank Manuel Richter for helpful discussions.

* Present address: School of Physics, Trinity College Dublin, Dublin 2, Ireland

¹ B. Shen, X. Deng, G. Kotliar, and N. Ni, Phys. Rev. B **93**, 195119 (2016).

² K. Yokoi, H. Murakawa, M. Komada, T. Kida, M. Hagiwara, H. Sakai, and N. Hanasaki, Phys. Rev. Mater. **2**, 024203 (2018).

³ Y. Luo, R. D. McDonald, P. F. S. Rosa, B. Scott, N. Wakeham, N. J. Ghimire, E. D. Bauer, J. D. Thompson, and F. Ronning, Sci. Rep. **6**, 27294 (2016).

⁴ D. Wu, J. Liao, W. Yi, X. Wang, P. Li, H. Weng, Y. Shi, Y. Li, J. Luo, X. Dai, and Z. Fang, Appl. Phys. Lett. **108**, 042105 (2016).

⁵ Y.-Y. Wang, Q.-H. Yu, P.-J. Guo, K. Liu, and T.-L. Xia, Phys. Rev. B(R) **94**, 041103 (2016).

⁶ Z. Yuan, H. Lu, Y. Liu, J. Wang, and S. Jia, Phys. Rev. B **93**, 184405 (2016).

⁷ A. Pariari, R. Singha, S. Roy, B. Satpati, and P. Mandal, Sci. Rep. **8**, 10527 (2018).

⁸ G. S. Saini, L. D. Calvert, and J. B. Taylor, Can. J. Chem. **42**, 630 (1964).

⁹ S. Furuseth, K. Selte, A. Kjekshus, S. Gronowitz, R. Hoffman, and A. Westerdahl, Acta Chem. Scand. **19**, 95

(1965).

¹⁰ I. A. Leahy, Y.-P. Lin, P. E. Siegfried, A. C. Treglia, J. C. W. Song, R. M. Nandkishore, and M. Lee, Proc. Natl. Acad. Sci. U.S.A. **115**, 10570 (2018).

¹¹ S. Zhang, Q. Wu, Y. Liu, and O. V. Yazyev, Phys. Rev. B **99**, 035142 (2019).

¹² D. Gresch, Q. Wu, G. W. Winkler, and A. A. Soluyanov, New J. Phys. **19**, 035001 (2017).

¹³ Y. Shao, Z. Sun, Y. Wang, C. Xu, R. Sankar, A. J. Breindel, C. Cao, M. M. Fogler, A. J. Millis, F. Chou, Z. Li, T. Timusk, M. B. Maple, and D. N. Basov, Proc. Natl. Acad. Sci. U.S.A. **116**, 1168 (2019).

¹⁴ F. Jin, X. Ma, P. Guo, C. Yi, L. Wang, Y. Wang, Q. Yu, J. Sheng, A. Zhang, J. Ji, Y. Tian, K. Liu, Y. Shi, T. Xia, and Q. Zhang, Phys. Rev. B **94**, 094302 (2016).

¹⁵ F. Arnold, C. Shekhar, S.-C. Wu, Y. Sun, R. D. d. Reis, N. Kumar, M. Naumann, M. O. Ajeesh, M. Schmidt, A. G. Grushin, J. H. Bardarson, M. Baenitz, D. Sokolov, H. Borrmann, M. Nicklas, C. Felser, E. Hassinger, and B. Yan, Nat. Commun. **7**, 11615 (2016).

¹⁶ K. Yoshida, J. Phys. Soc. Jpn. **41**, 574 (1976).

¹⁷ K. Yoshida, J. Phys. Soc. Jpn. **40**, 1027 (1976).

¹⁸ K. Yoshida, J. Appl. Phys. **51**, 4226 (1980).

- ¹⁹ D. Shoenberg, Magnetic Oscillations in Metals (Cambridge University Press, 1984).
- ²⁰ K. Koepnik and H. Eschrig, Phys. Rev. B **59**, 1743 (1999).
- ²¹ J. P. Perdew, K. Burke, and M. Ernzerhof, Phys. Rev. Lett. **77**, 3865 (1996).
- ²² R. Ling and C. Belin, CR Acad. Sci. Paris **292**, 891 (1981).
- ²³ C. Xu, J. Chen, G.-X. Zhi, Y. Li, J. Dai, and C. Cao, Phys. Rev. B **93**, 195106 (2016).
- ²⁴ J. Sun and D. J. Singh, J. Appl. Phys. **121**, 015101 (2017).
- ²⁵ Note that in Ref.¹, calculations are shown both for the primitive and the conventional unit cell, but only the former will produce a correct band structure²⁶.
- ²⁶ A. Yaresko, A. P. Schnyder, H. M. Benia, C.-M. Yim, G. Levy, A. Damascelli, C. R. Ast, D. C. Peets, and P. Wahl, Phys. Rev. B **97**, 075108 (2018).